Unveiling the distinct structure of the upper mantle beneath the Canary and Madeira hotspots, as depicted by the 660, 410 and X discontinuities

Luciana Bonatto[1], David Schlaphorst[2], Graça Silveira[2], João Mata[2], chiara cciviero[3], Claudia Piromallo[4], and Martin Schimmel[5]

[1]Universidad de La Serena
[2]Faculdade de Ciências, Instituto Dom Luiz (IDL)
[3]Instituto de Ciencias del Mar
[4]Istituto Nazionale di Geofisica e Vulcanologia
[5]Geosciences Barcelona

March 07, 2024

Unveiling the distinct structure of the upper mantle beneath the Canary and Madeira hotspots, as depicted by the 660, 410 and X discontinuities

Luciana Bonatto [1], David Schlaphorst[2], Graça Silveira[2,3], João Mata[2], Chiara Civiero[4,5], Claudia Piromallo[6], Martin Schimmel[7]

[1]Departamento de Física de la Universidad de La Serena, Av. Juan Cisternas, 1200, La Serena, 1700000, Coquimbo, Chile
[2]Faculdade de Ciências, Instituto Dom Luiz (IDL), Universidade de Lisboa, Campo Grande, 1749-016, Lisbon, Portugal
[3]Instituto Superior de Engenharia de Lisboa, Rua Conselheiro Emídio Navarro 1, Lisbon, 1959-007, Portugal
[4]Institut de Ciències del Mar, ICM-CSIC, Pg. Marítim de la Barceloneta, 37, Barcelona, 08003, Spain
[5]Dipartimento di Matematica, Informatica e Geoscienze, Università di Trieste, via Weiss 2, Trieste, 34128, Italy.
[6]Istituto Nazionale di Geofisica e Vulcanologia, Via di Vigna Murata, 605, Rome, 00143, Italy
[7]GeoSciences Barcelona, Geo3Bcn, CSIC, c/ Solé Sabarís sn, Barcelona, 08028, Spain

Key Points:

- We investigate mantle transition zone and X discontinuity structure below Canary and Madeira using P receiver functions
- Deeper 410 in both, shallower 660 in Canaries, normal in Madeira. Suggests Canary plume crosses MTZ, Madeira plume affects upper MTZ.
- Detection of X discontinuity suggests a deep-rooted thermochemical plume.

Corresponding author: Luciana Bonatto, albonatto@gmail.com

Abstract

The Canary and Madeira Islands are two distinct hotspots in the Central-East Atlantic that are close to each other. Their volcanism is generally attributed to underlying mantle plumes, but the detailed structure of these plumes is still not well understood. The thermal and compositional structure of the plume introduces complexities in the phase transitions of the mantle, which impact the depth and magnitude of seismic discontinuities. We use 1268 high-quality receiver functions from stations located at the two hotspots to detect P-to-s converted phases through a common-conversion point stacking approach and conduct a detailed analysis of mantle seismic discontinuities. The results show that both hotspots are characterized by a thin mantle transition zone (MTZ), with sharp 410 and 660 discontinuities at depths of 429-420 km and 647-664 km, beneath the Canaries and Madeira respectively. The results indicate that the Canary plume crosses the MTZ, whereas the Madeira plume mainly influences the upper portion of the MTZ. Furthermore, we find reliable detections of a sharp X discontinuity beneath the Canaries at 289 km. Its presence suggests the accumulation of silica-rich recycled eclogite at these depths. We also use the amplitudes of P410s and PXs to derive velocity jumps at corresponding discontinuities. Based on these measurements, we estimate that the basalt proportion is 60-80%, with accumulation being more significant in the Canaries than in Madeira. The MTZ thickness, the presence of the X discontinuity, and the high basalt proportion provide compelling evidence for a deep-rooted thermochemical plume beneath the study area.

Plain Language Summary

We examine the Canary and Madeira Islands, two separate groups of islands in the Atlantic Ocean, close to each other. While it is generally accepted that volcanic activity in these regions is driven by underlying mantle plumes, the precise characteristics of these plumes remain relatively unknown. Tomography studies have revealed distinct structures of the plumes, with the Canary plume extending vertically throughout the upper mantle, while the Madeira plume is visible up to a depth of 300 km, beyond which the resolution of the images deteriorates. We use receiver functions, derived from the analysis of seismic waveforms, particularly the conversion of compressional waves to shear waves at seismic discontinuities within the Earth. Receiver functions offer a higher resolution compared to tomographic images, primarily due to their ability to directly measure seismic wave conversions at specific depths, reflecting where mantle minerals change their crystal structure. This analysis provides insights into the variations in temperature and mineral chemistry in the mantle, as both factors influence the depths of crystal rearrangements. Our research provides evidence supporting the existence of a deep-seated thermochemical plume beneath the study area. However, beneath Madeira, the plume may be less vigorous or presently disconnected from its deep source.

1 Introduction

The Canary and Madeira archipelagos are part of two intraplate volcanic provinces in the Central-East Atlantic Ocean close to the African coast (Figure 1). Both provinces consist of linear chains of volcanic islands and seamounts that display a general SW-NE progression of increasing volcanism age, aligning with the movement of the African plate. They are both marked by relatively low-magnitude seismic activity, which on the Canaries is mainly associated with volcanic processes (Carracedo & Troll, 2021). Although still under debate, the volcanism of both archipelagos is attributed to the interaction between the African Plate and underlying mantle plumes (Mata et al., 1998; Geldmacher et al., 2001, 2005; Civiero et al., 2021; Negredo et al., 2022).

The most recent travel-time tomography models image slow anomalies under both archipelagos, attributed to mantle upwellings (Civiero et al., 2018; Civiero, Custódio, et

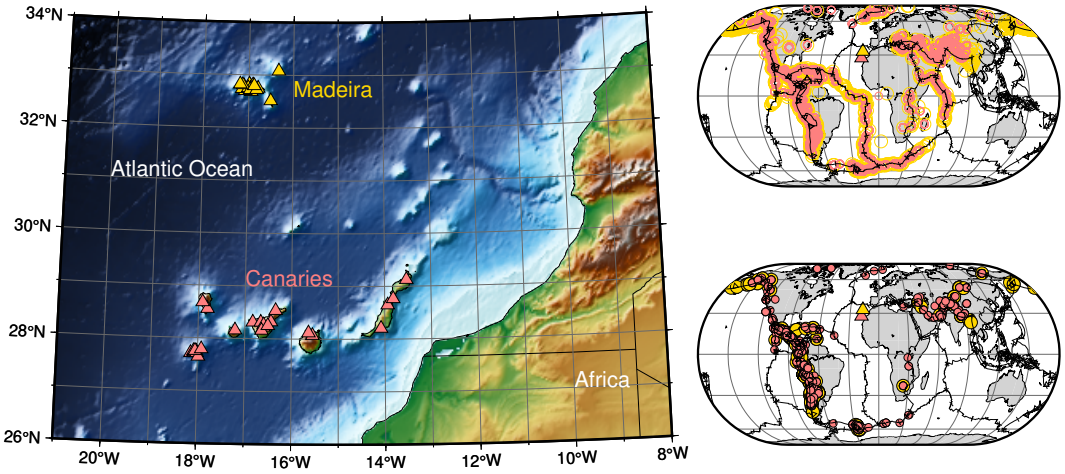

Figure 1. Map of the Canary and Madeira archipelagos displaying station locations (left), with yellow and red triangles representing stations in Madeira and the Canaries, respectively. On the right, the global distribution of all teleseismic earthquakes recorded in the seismic stations (top) and the ones used in the final analysis (bottom) after rigorous quality controls, with red triangles marking the positions of the Madeira archipelago and green for the Canary archipelago. Events follow the same color coding as the triangles, with green indicating events analyzed for the Canaries and red for those related to Madeira.

al., 2019). In a recent comprehensive analysis employing tomography and paleo-reconstruction models, Civiero et al. (2021) proposed that both the Madeira and Canary hotspots are fed by plume-like structures overlying the seismically slow Central-East Atlantic Anomaly (CEAA). This anomaly emerges from depths below 700 kilometres and maintains a connection with the African LLSVP (Large Low-Shear-Velocity Province). However, the two hotspot systems seem to be in different stages of development. According to this model, while the Canary plume-like structure is rooted in the CEAA, tomography results hint that the small Madeira plumelet (100 km width) appears detached from it. The plumelet extends from the surface down to at least 300 km, below which the resolution degrades. The presence of mantle upwellings beneath the Canary and Madeira archipelagos is also supported by new shear-wave splitting measurements (Schlaphorst et al., 2022). However, in the Canary Province many of the predictions of plume theory (Morgan, 1972) are not met, e.g., volcano ages do not follow a consistent linear age–distance relationship, with coeval volcanism occurring across several hundreds of kilometres (Geldmacher et al., 2001, 2005). Insights from numerical modelling of mantle flow highlight the potential role of edge-driven convection in deflecting the mantle plume beneath the Canary archipelago, providing a plausible explanation for the complex age progression of the magmatism and widespread volcanism (Negredo et al., 2022; Manjón-Cabeza Córdoba & Ballmer, 2022).

Studying the seismic discontinuities beneath both hotspots can provide new insights into the mantle thermal and compositional properties of these regions, thus allowing the assessment of the origin of these hotspots. Seismic discontinuities mark discernible changes in the density, shear and compressional wave speeds of the mantle as depth increases. The occurrence, depth and seismic visibility of these changes are dependent on the temperature and composition variability of the mantle. The upper mantle has predominantly peridotite composition, where the dominant mineral is olivine, usually corresponding to more than 50% volume, accompanied by orthopyroxene and, in most fertile compositions, by clinopyroxene and an aluminous phase that changes with pressure (e.g., Ziberna et

al., 2013, and references therein). This dominant peridotite composition contains dispersed eclogite domains, resulting from recycling altered oceanic crust into the mantle via subduction (e.g., Allègre & Turcotte, 1986; Helffrich & Wood, 2001). Such predominant olivine-rich parageneses change in depth as a result of several phase transitions (PT) that explain the observations of sharp seismic discontinuities at the base of the upper mantle: at a depth of 410 km olivine transforms to wadsleyite (ol→wa) with a positive Clapeyron slope, at 520 km wadsleyite transforms to ringwoodite (wa→ri) with a positive Clapeyron slope and at 660 km ringwoodite dissociates into bridgmanite ((Mg, Fe)-perovskite) and magnesiowustite (ri→br+mw) with a negative Clapeyron slope (e.g., Helffrich, 2000; Helffrich & Wood, 2001). The corresponding seismic discontinuities are named 410, 520 and 660, after the approximate depth at which the PT occur. The region of the mantle bounded by the 410 and 660 is known as the Mantle Transition Zone (MTZ).

The thermal and compositional structure of the mantle introduces complexities in the PT. Temperature anomalies in the mantle move the PT to different pressures (depths) according to their respective Clapeyron slopes (Bina & Helffrich, 1994). Due to the opposite sign in the Clapeyron slopes of the PT responsible for the 410 and 660, the depth changes of these discontinuities are anti-correlated in response to a thermal anomaly. Therefore, while the 410 becomes shallower in colder regions and deeper in hotter ones, the depth changes of the 660 are opposite. Consequently, the MTZ is expected to be thicker when crossed by subducted slabs and thinner in high temperature regions (Vidale & Benz, 1992; Collier & Helffrich, 2001; Helffrich, 2000; Lawrence & Shearer, 2006). This expected behaviour of the MTZ has been used as an indication of thermal anomalies, akin to a mantle thermometer (e.g., Helffrich, 2000).

Variations in composition and temperature may lead to other mineral phase transformations introducing further complexities in the structure of the MTZ and the mantle above. For example, at extremely high temperatures, perovskite may appear at 660-700 km by a PT involving majorite garnet, which is thought to be, at those conditions, the dominant mineral phase at the MTZ (Weidner & Wang, 1998; Hirose, 2002; Yu et al., 2011; Liu et al., 2018). The majorite garnet PT has a positive Clapeyron slope, which contrasts with the positive slope of the ringwoodite PT. As a result, in a hot mantle, the 660 would occur at greater depths. This could lead to a positively correlated depressed topography on the 410 and 660 discontinuities with a minor overall impact on the thickness of the MTZ (Deuss et al., 2006; Deuss, 2007). Furthermore, this PT occurs across a broad depth interval, significantly broadening the 660 discontinuity. Moreover, the role of aluminum on the stability fields of ringwoodite and majorite garnet has been a subject of debate (Weidner & Wang, 1998; Yu et al., 2011).

Additionally, mantle upwellings rooted deep in the mantle not only exhibit high temperatures but also different composition from the surrounding mantle. As part of mantle convection, cold, ancient oceanic crust is transformed into eclogite in subduction zones, transported to the lower mantle and then is brought back up into the upper mantle once entrained in hot mantle plumes. Because of their unique chemical signature, these plumes are known as thermochemical plumes rather than purely thermal plumes (see Koppers et al. (2021) for a review). The presence of a consistent seismic discontinuity approximately 300 km beneath various hotspots is considered strong evidence of the thermochemical nature of deep-seated plumes (Schmerr, 2015; Kemp et al., 2019; Pugh et al., 2021). This discontinuity named the 300 or X discontinuity, is attributed to the coesite-to-stishovite (co→st) phase transition in regions of the mantle enriched in eclogite (Williams & Revenaugh, 2005), as expected for a thermochemical plume.

Receiver functions and precursor studies have examined the MTZ beneath the Canary Islands at a regional scale, while those from Madeira are contributions from global studies. In the Canaries, studies indicate a thinner MTZ, possibly due to hot mantle material (Deuss, 2007; Martinez-Arevalo et al., 2013; Saki et al., 2015). For Madeira, studies show a moderately thinner MTZ, supporting the plume theory (Houser et al., 2008;

Lawrence & Shearer, 2008; Deuss, 2009). However, a detailed analysis of MTZ discontinuities is lacking in both regions, especially for Madeira.

In this study, we investigate the fine structure of the upper mantle and MTZ beneath both archipelagos using receiver functions. In particular, we estimate the time, amplitude and frequency content of P-to-s converted phases from which we derived the depth, magnitude and width of velocity jumps of mantle discontinuities. Through a comprehensive interpretation of our findings in the context of mineral physics and geodynamics, we inferred the thermochemical nature of the Canary mantle plume. Beneath Madeira, our findings confirm the observations from Civiero et al. (2021) suggesting that the plume appears to be disconnected from the lower mantle and primarily affects the upper portion of the MTZ.

2 Data

For the Canary archipelago, we use data from 23 stations of the Spanish Digital Seismic Network (operated by the *Instituto Geográfico Nacional*) and one station from the Global Seismograph Network. These stations were active in varying periods, ranging from 2008 to 2017. For Madeira, we use data from 16 stations from the temporary DOCTAR network that was active during 2011/2012 (Matos et al., 2015), as well as 2 permanent stations of the Portuguese National Seismic Network (Instituto Português do Mar e da Atmosfera, I.P., 2006). of those stations are short-period, so we removed the instrument response before the processing. See Figure 1 for station deployment and Table S1 in the supporting material for names and geographic coordinates of stations.

We selected the waveforms of 1241 events for the Canary archipelago and 1268 events for Madeira, of Mw between 5.5 and 7 and from epicentral distances between 30° and 95°. After discarding incomplete ZNE triplets, we obtain 13578 three-component waveforms for the Canary archipelago and 6481 for Madeira.

3 Method

To investigate the structure of the upper mantle, we employ receiver functions (RFs) and common conversion point stacking techniques.

3.1 Receiver functions

We use teleseismic *Pds* phases, i.e. the phases resulting from the direct P wave converting to an S wave at a seismic discontinuity at a depth d. Because of their polarization and their almost vertical incidence, *Pds* conversions are recorded on the radial (R) component of teleseismic earthquakes. The direct detection of *Pds* phases in individual seismograms is challenging due to their weak amplitude and their arrival during the coda of the P phase, which is marked by numerous other phases, including multiple reflections and scattered waves. However, converted phases are expected to be coherent with the waveform of the main P arrival for conversion at discontinuities which are thinner than one-half of the P-wavelength (Richards, 1972; Paulssen, 1988; Bostock, 1999). Therefore, it is possible to extract them by waveform similarity. This can be done using deconvolution of the P phase in the vertical component (P_Z) from R, which is known as the receiver function (RF) technique (Phinney, 1964; Vinnik, 1977; Langston, 1979; Ammon, 1991). The deconvolution process eliminates the source component and isolates the P-to-s conversion peaks from discontinuities beneath the station.

We compute RFs using the processing methods outlined in Bonatto et al. (2015, 2020). The processing workflow is illustrated in Figure 2a and described in detail in Supporting material Section 1. After the processing and the quality controls, we obtain 948 RFs for the Canaries and 320 RFs for the Madeira archipelago in five frequency bands:

0.02-0.12 Hz, 0.02-0.2 Hz, 0.02-0.32 Hz, 0.02-0.48 Hz, 0.02-0.64 Hz. Table S1 summarises the number of teleseismic records per station and the corresponding final number of good-quality RFs.

3.2 Stacking of receiver functions with moveout correction

During the stacking process, we apply a linear moveout correction, also known as a slowness stack, to account for the time delay between the arrival of seismic waves at different distances from the source. This correction ensures that the seismic signals are accurately aligned and stacked, resulting in improved signal detection and identification.

To perform the stacking process with a linear moveout correction, we use two techniques: the phase weighted stack (PWS) (Schimmel & Paulssen, 1997) and the linear stack (LS). The PWS is a non-linear stacking technique that incorporates the coherence of the instantaneous phase as a weight in the linear stack, enhancing the signal-to-noise ratio (SNR) and improving the accuracy of signal detection.

The stacking process with moveout correction, accounting for both stacking techniques, is applied as follows:

$$S(s_j, t) = \frac{1}{N} \sum_{i=1}^{N} RF_i(t + s_j(\Delta_i - \Delta_{REF}))c_i \tag{1}$$

where s_j refers to a specific relative slowness with respect to the P phase, t is relative time with respect to the P phase, Δ_i is the epicentral distance for RF_i, Δ_{REF} is the reference epicentral distance, and N is the total number of stacked RFs. The reference distance, Δ_{REF}, of 75° is chosen for all the slowness stacks to account for the distribution of epicentral distances which are mainly concentrated between 60° and 90°.

The weight c_i in equation 1 is the phase stack and it accounts for the instantaneous phase similarity:

$$c_i = |\frac{1}{N} \sum_{k=1}^{N} e^{i\phi_k(t+s_j(\Delta_i-\Delta_{REF}))}|^{\nu} \tag{2}$$

ϕ_k is the instantaneous phase for the k-th RF, and the parameter ν controls the weighting of phase similarity and dissimilarity. The move-out corrected LS is defined with $\nu = 0$ ($c_i = 1$), while for the PWS we choose a value of $\nu = 2$.

3.2.1 Identification of converted phases in global stacks

The average fine structure of the upper mantle in the study area is obtained by stacking all the RFs that passed the quality controls in the lowest frequency band (0.02−0.12 Hz). This global stack is useful for identifying converted phases from major discontinuities and from minor reflectors that are prevalent throughout the area.

Figures 3 a and b display relative time-distance stacks of RFs for the Canaries and Madeira datasets, respectively, with the P phase set as time zero. Each trace at a given epicentral distance is computed from the stack (PWS) of RFs with epicentral distances within a 5° interval and uses a fixed relative slowness parameter of −0.1 s/° to perform the move-out correction within that distance interval. Since converted phases have a steeper angle of incidence than the direct P phase, Pds phases are always expected to align along a negative slope line (i.e., negative relative slowness), as shown with the continuous black lines. Conversely, multiples have a shallower angle of incidence and a corresponding positive slope (i.e., positive relative slowness), as shown with the dashed lines. Slowness stacks,

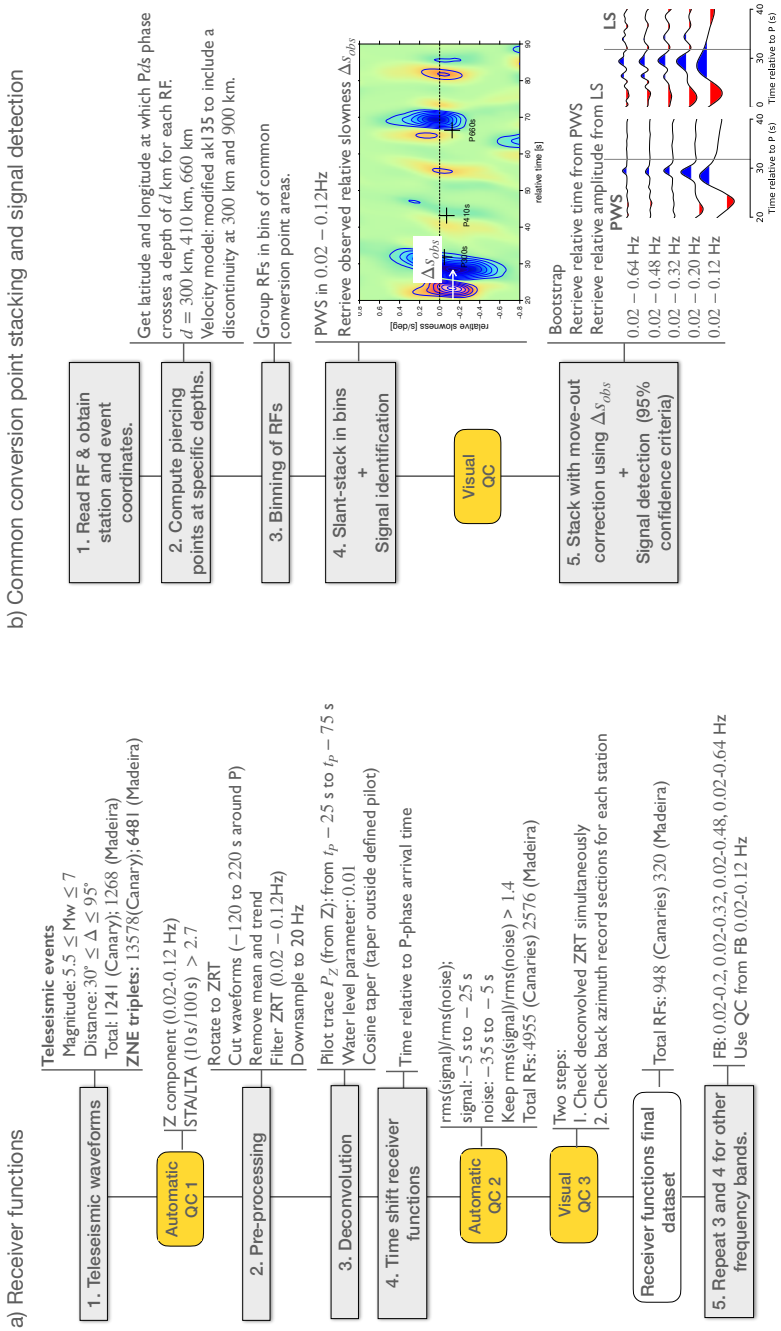

Figure 2. Processing workflow of a) Receiver functions and b) Common conversion point stacking of RFs.

also referred to as vespagrams or relative time-slowness stacks, are a useful tool for unambiguously identifying Pds phases. Figure 3 c and e show the slowness stacks for the Canary dataset and Figure 3 d and f show the slowness stack for the Madeira dataset. Here, all RFs are stacked applying a linear move-out correction for a range of slowness values and the result is plotted in the relative time-slowness domain, where the reference at zero is the P phase. Conversions from discontinuities in the upper mantle are expected with negative relative slowness, while multiples are expected with positive relative slowness.

3.2.2 Common conversion point stacking and signal detection

The lateral variations of the detected discontinuities are investigated using a common-conversion-point (CCP) stacking approach as in Bonatto et al. (2020). The processing workflow for the CCP stacking and signal detection is illustrated in Figure 2b. We first retrieve station and event coordinates for each RF (step 1, Figure 2b) and compute piercing points of converted phases $P300s$, $P410s$ and $P660s$ at their respective conversion depths: 300 km, 410 km, and 660 km (step 2, Figure 2b). The CCP stacking is performed for these three conversion depths, which correspond to the reference depth of our target discontinuities. For each conversion depth, we stack the RFs with conversion point coordinates in the same circular area or bin (step 3, Figure 2b). To ensure reliable measurements, we set the bin radius at each conversion depth to match the size of the first Fresnel Zone at an intermediate frequency of 0.2 Hz: $r_{P300s,P410s} = 0.5°$ and $r_{P660s} = 0.75°$. The centres of these bins are spaced equally at intervals of 0.7° to enable an overlap of the sampled areas. Notice that even with the smallest bin radius of 0.5°, the 0.7° interval permits an intentional overlap of 0.3°. If the number of RFs in the bin is less than 25, we increase the bin radius to $r_2 = 1.5r_{Pds}$, or to $r_3 = 2r_{Pds}$ if numbers remain low. After stacking the RFs in each bin and conversion depth, we perform a visual quality assessment of individual slowness stacks within the lowest frequency band of 0.02−0.12 Hz (step 4, Figure 2b). We allocate a quality level from 1 to 3 for each stack, based on these criteria:

1: The signal identification is very clear, without other signals near the target phase.
2: Other coherent signals near the target phase, but the signal is still clear.
3: Multiple coherently stacked signals of similar amplitude near the target signal or non-detection.

Representative examples of stacks classified as quality 1, 2, and 3 for P300s are shown in Figs. S1 to S11 of Supporting material Section 2. Stacks with quality 1 and 2 are considered as good quality stacks and stacks of quality 3 are not considered in the analysis.

We use the good quality stacks to estimate the relative slowness at which each phase is detected. Then, for each frequency band (0.02-0.12 Hz, 0.02-0.2 Hz, 0.02-0.32 Hz, 0.02-0.48 Hz, 0.02-0.64 Hz), we compute the stacking with move-out correction (step 5, Figure 2b) using this slowness value; i.e., fixed s_j in Eq. 1. The final stacks are calculated using a bootstrap resampling algorithm of 20 repetitions with replacement (i.e., a waveform may be chosen multiple times). The bootstrap method enhances our statistical analysis. This approach involves constructing a distribution of stacked RFs for each CCP bin by resampling and stacking numerous subsets of data. This approach fulfils two key objectives: first, it mitigates the influence of outliers by diluting the effect of any individual RF with an anomalously large amplitude across multiple bootstrap iterations. Second, it promotes the reliable detection of any consistent feature within the stacks, regardless of its magnitude. The recurrence of any distinctive pattern within the bootstrap samples strongly indicates the presence of a genuine geophysical feature, rather than merely being the result of data variability. Moreover, this method enables us to perform a thorough evaluation of the statistical significance of the RF amplitude observations.

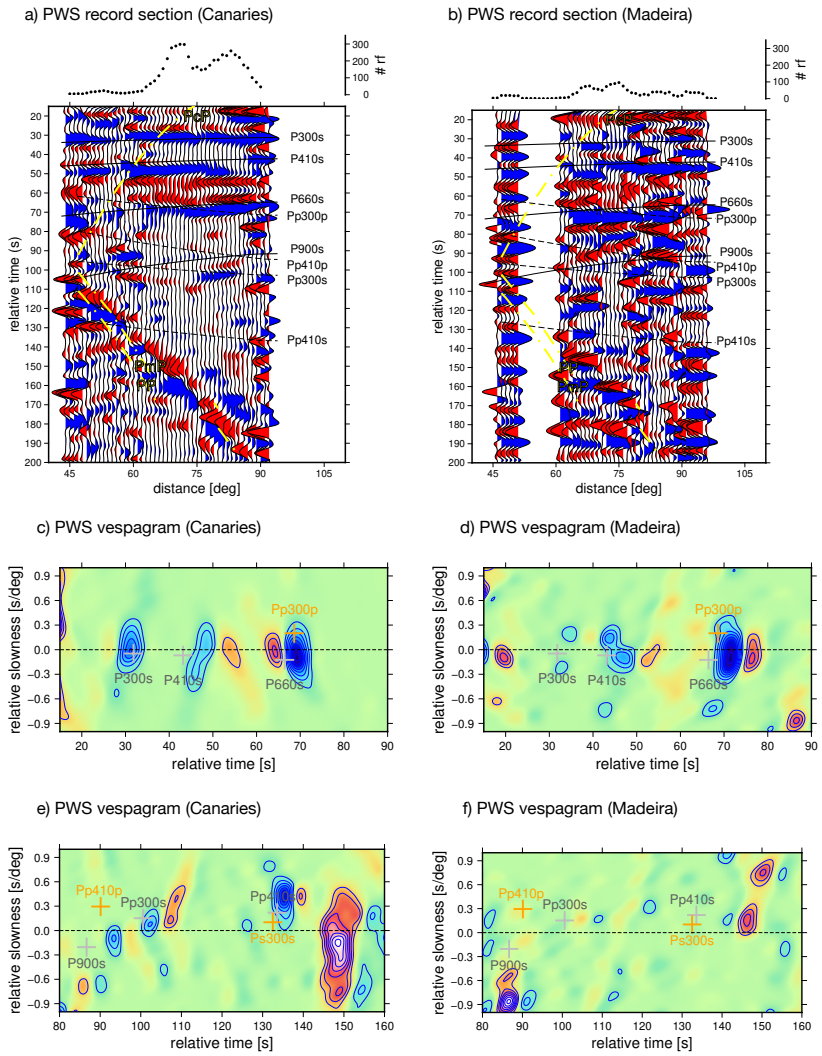

Figure 3. Record sections for (a) the 948 RFs from the Canary Island dataset and (b) the 320 RFs from the Madeira dataset. Each trace in the record sections results from stacking (PWS) the RFs with epicentral distances within a 5° interval around a given epicentral distance in the horizontal axis. Blue and red colours represent positive and negative amplitudes. Black lines show the theoretical travel time curves for a slightly modified ak135 reference model that includes imperceptible density increase at 300 km and 900 km. Dashed yellow lines represent travel time curves for potentially interfering phases (PcP, PmP, PP). The number of RFs is indicated at the top of the record section. (c)-(f) Stacking (PWS) in the relative time-slowness domain for the Canaries and Madeira dataset in different time intervals. Crosses mark the expected time and slowness of different phases for positive (gray) and negative polarities (orange) in the modified ak135 reference model.

We measure the relative travel time values from the PWS and the amplitude of converted phases from the LS. We only include signals in the analysis that meet the 95% confidence criteria, which requires the amplitude of a detected signal to be at least twice its amplitude standard error. Finally, we retain only those detected signals from good-quality stacks (quality levels 1 and 2) with more than 25 stacked RFs. These detections should also show negative slowness and positive amplitude, as expected for the target-converted phases.

3.3 Time-to-depth conversion

To convert relative times to depth, we use tomography-derived velocities. Velocity anomalies are extracted from two tomography models: the global model MIT08 (Li et al., 2008) and the regional model IBEM-P18 (for P waves)/IBEM-S19 (for S waves) (Civiero et al., 2018; Civiero, Custódio, et al., 2019). While the regional model has a higher resolution, it does not cover the entire area of interest. However, we include it in the analysis to assess the consistency of the results in the overlapping region with both models. Since MIT08 only accounts for P-wave anomalies, we approximate corresponding S-wave anomalies to be 1.3 times P-wave anomalies at the surface, increasing linearly to 3 times at the base of the mantle, following Ritsema and Van Heijst (2002). To account for possible resolution overestimation given by noiseless synthetic tests (Li et al., 2008; Civiero, Armitage, et al., 2019), we assume that the amplitudes of anomalies recovered by the inversion could be about 50% than those of unknown real anomalies. Therefore, we compute the corrections using MIT08 and IBEM-P18/S19 anomalies multiplied by a factor of 2.

For each tomography model, we compute time corrections for each CCP bin and converted phase. We use TauP toolkit (Crotwell et al., 1999) to create a modified *ak135* velocity model for each bin which includes the anomalies. We use this new velocity model to compute the theoretical relative travel times of converted phases (for a reference distance of 75°). Then, we use these relative travel times to compute time corrections with respect to *ak135*, i.e., the difference between travel times obtained with ak135 and with the modified ak135. Finally, we add the correction to the observed relative times of detected signals and the corrected time values are converted to depth using the reference velocity model *ak135* for a reference distance of 75°. Although the tomographic models used to compute the corrections have large uncertainties, it should be noted that the overall effect of the corrections is to locate the discontinuities closer to their actual depth.

3.4 Temperature variations in the MTZ

The thickness of the MTZ at each location is calculated by subtracting the depths of the 410 and 660 discontinuities ($z_{660} - z_{410}$). Variations in the MTZ thickness can be attributed to temperature variations, as thermal anomalies affect the depths of the 410 and 660 discontinuities differently.

The conversion of anomalous MTZ thickness to temperature is accomplished through the use of Clapeyron slopes associated with the olivine phase transitions (refer to Table S2). Clapeyron slopes (dP/dT or γ) can be written as

$$\left(\frac{dP}{dT}\right)_H \approx \frac{dP}{dz}\frac{\delta z_H}{\delta T} \tag{3}$$

where H stands for 410 or 660, δz_H corresponds to $\delta z_{410} = 410 - z_{410}$ or $\delta z_{660} = 660 - z_{660}$ and dP/dz is the upper-mantle pressure increase with depth which is about 100/3 MPa km^{-1} in *PREM* (Dziewonski & Anderson, 1981).

As proposed by Helffrich (2000), we adopt the assumption that the deflection of discontinuities is due to vertically consistent temperature changes. Therefore, we can convert the difference in MTZ thickness to temperature variation using the equation below

$$\delta T = \left[\left(\frac{dP}{dT} \right)_{660} - \left(\frac{dP}{dT} \right)_{410} \right]^{-1} \frac{dP}{dz} \, \delta MTZ \tag{4}$$

where $\delta MTZ = MTZ_{thickness} - 250$ km or $\delta MTZ = MTZ_{thickness} - 242$ km, if we consider the reference value for the MTZ thickness from the global RFs study of Lawrence and Shearer (2006).

3.5 Frequency and amplitude analysis of converted phases

Studying the seismic visibility and the amplitude of seismic phases provides important constraints on the sharpness and velocity contrast of the velocity gradients associated with mantle discontinuities. (Shearer & Flanagan, 1999; van der Meijde et al., 2003; Juliá, 2007; Bonatto et al., 2020; Pugh et al., 2021). These parameters and the discontinuity depth are directly linked to the underlying mechanisms that give rise to the seismic boundaries and play an important role in interpreting our observations.

3.5.1 Sharpness of discontinuities

Seismic discontinuities are generally approximated as linear velocity gradients, which act as a low pass filter to converted waves. In particular, the amplitudes of the converted waves at the discontinuity are significant when the gradient transition interval, Δz, is smaller than half of the wavelength, λ_P, of the incident P-wave (Bostock, 1999; Paulssen, 1988). This is

$$\Delta z < \frac{\lambda_P}{2} = \frac{v_P}{2f} \tag{5}$$

where v_p is the P-wave velocity at the corresponding discontinuity depth. Therefore, to constrain the thickness of discontinuities, we need to find the highest frequency f^{max} for which the amplitude of converted phases is visible. We estimate this frequency value by analyzing the amplitudes of converted phases in the CCP linear stacks across the different frequency bands that we use to compute the RFs. We use the following criteria: f^{max} is the frequency above which the amplitude drops below 50% of the amplitude at the lowest frequency. Finally, the upper bound for the thickness of the discontinuity is obtained by substituting f with f^{max} in Eq. 5. This rule of thumb has been used before to constrain the thickness of mantle discontinuities (e.g., Paulssen, 1988; Bostock, 1999; van der Meijde et al., 2003; Jenkins et al., 2017; Bonatto et al., 2020).

3.5.2 Velocity contrast

Reflection and transmission coefficients describe how the energy of a seismic wave is partitioned when it encounters a boundary between two elastic media. They are obtained as the amplitude ratio of the incoming wave and the reflected or transmitted waves. The coefficients depend on several factors, including the velocities and densities of the seismic waves on both sides of the interface (the velocity and density contrasts), and the angle of incidence of the incoming wave. The elementary formulas to compute the coefficients can be found in equations 5.39 and 5.40 of Aki and Richards (2002).

To estimate the velocity contrast across each detected discontinuity, we manually compare the theoretical coefficients of converted phases, assuming different velocity contrasts, with the estimated amplitudes of the *Pds* phases in our stacked RFs. This comparison allows us to obtain a rough assessment of the velocity jump. To minimize atten-

uation effects due to the finite thickness of discontinuities, we perform this analysis for RFs in the lower frequency band: 0.02-0.2 Hz. In this approach, we assume that *Pds* phases are primarily sensitive to S-wave velocity contrasts, as demonstrated by Juliá (2007).

4 Results

We investigate the upper mantle and MTZ structure using 948 high-quality RFs around the Canaries and 320 around Madeira. We first create time-distance stacks and vespagrams for the entire dataset of each archipelago to identify converted phases of possible discontinuities prevalent throughout the area.

The number of events observed at stations in the Canary archipelago that pass the quality controls are higher across almost the entire distance range, resulting in stronger signals of the major converted phases in the time-distance stacks (Figures 3 a, b). The vespagrams confirm that we obtain clear converted phases from the globally detected 410 and 660 discontinuities beneath both volcanic provinces (Figures 3 c, d). However, a clear converted phase at a reflector near 300 km depth is only observed beneath the Canaries. Based on the robust detections of the 410 and 660, we have confidence that this measurement of the X discontinuity is not an anomaly caused by data coverage. In contrast to the Canary archipelago, no strong multiples (Pp300s and Pp410s) from the reflectors at the X and 410 discontinuities can be observed around the Madeira archipelago (Figures 3 e, f). Likewise, a converted phase at a discontinuity of approximately 800-900 km depth can be observed around the Canaries but is not present around Madeira. This phenomenon will be subject to further investigation in a future study.

4.1 Topography of discontinuities and MTZ thickness

To investigate the spatial distribution of the converted phases, we apply the CCP stacking method. Figure 4 shows the CCP bins where converted phases were reliably detected. Then, we use the relative times of the converted phases to estimate the depth of the discontinuities from tomography-derived velocities with the global model MIT08 (Li et al., 2008).

Our analysis indicates that the X discontinuity is situated at a mean depth of 288±6 km ($\bar{x}\pm1\sigma_{\bar{x}}$) beneath the Canaries (Figure 5), with a range spanning from 251 km to 316 km. It is prominent around the western and central part of the Canaries with depths shallower than 300 km towards the south and deeper than 300 km towards the north (Figure 6a), likely stemming from a larger azimuthal coverage from the west and south. For Madeira, we have only retained one reliable detection of this discontinuity in the west, with a depth of 313 km.

On average, the 410 is located deeper beneath the Canaries (Figure 5) with a mean depth of 428±4 km and a range of 403 km to 448 km, in comparison to a mean depth of 421±3 and a range of 407 km to 428 km beneath Madeira. Whereas in the Canaries it is located deeper towards the western part of the archipelago with values larger than 410 km southwest of the islands of La Palma, Tenerife and Gran Canaria, and smaller values to the northeast, a lateral trend is not as evident around the Madeira archipelago (Figure 6 b). This difference can be attributed to Madeira's smaller geographical extent compared to the Canaries, as well as the fact that the stations collectively cover a significantly smaller area. We observe, larger values in the northwest and a shallower value towards the south, making this pattern less pronounced.

In contrast, the 660 is shallower towards the east of the Canary archipelago with a mean depth of 647±2 km and ranges of 625 km to 675 km, in comparison to a mean depth of 664±3 km and a range of 637 km to 687 km beneath Madeira. Based on the piercing point distribution, nearly all results can be found towards the west of Madeira

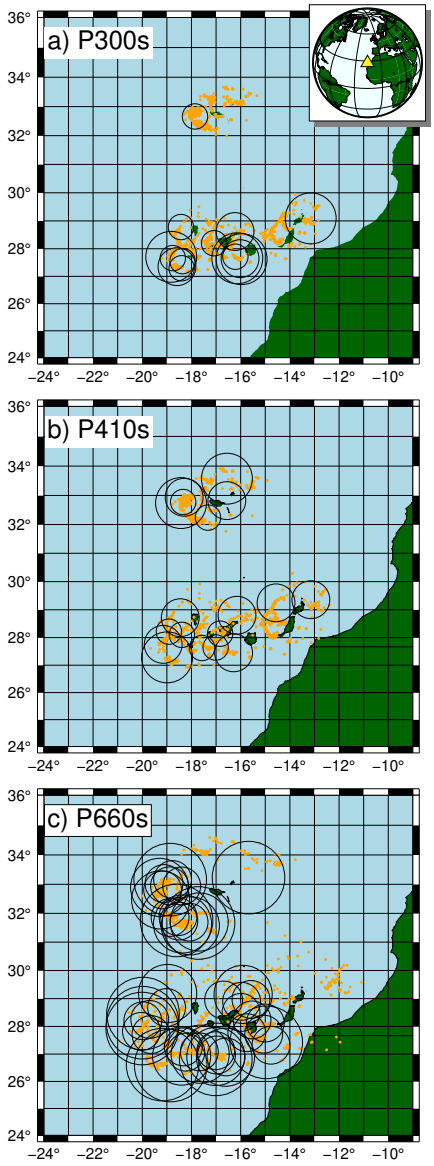

Figure 4. Location of common conversion point bins with robust detections (with PWS and LS) of the converted phases: a) P300s, b) P410s, and c) P660s. Circles correspond to CCP bins with signals that satisfy the 95% confidence criteria. The size of the circles are proportional to the radius of the CCP bin; from the smallest to the largest, the radii of the circular sectors are: 0.5°, 0.75°, 1.0°, 1.25°, 1.5°. Orange dots indicate the piercing points of corresponding phases.

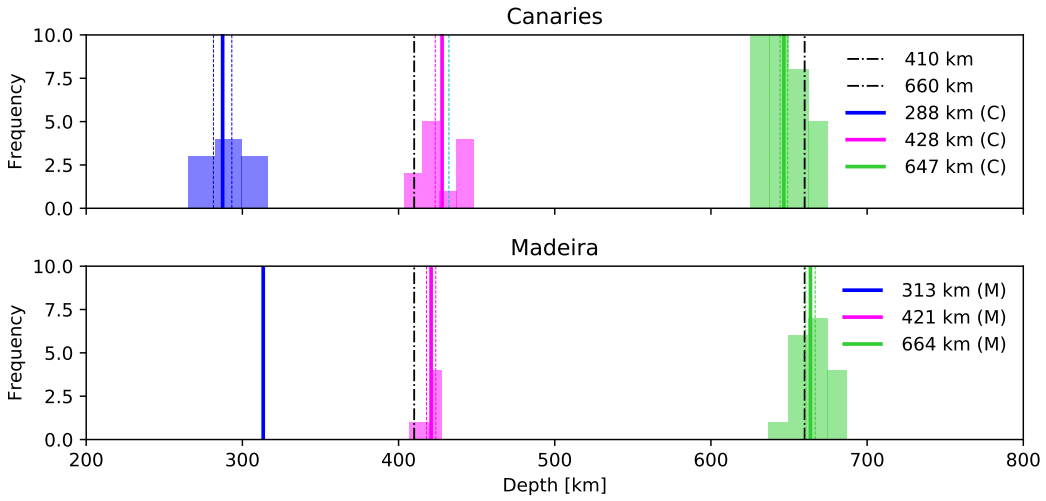

Figure 5. Histograms of estimated depth values, after time corrections, for the X, 410, and 660 discontinuities beneath the Canaries and Madeira. Vertical solid lines (blue, pink, green and black) correspond to mean depth values for both archipelagos (given in the legend, where M stands for Madeira and C for the Canaries), dashed lines correspond to standard errors of mean values and dash-dotted lines are reference depth values in a modified ak135 model that incorporates a discontinuity at 300 km.

and around the western and central part of the Canaries (Figure 6c). In Madeira, the 660 is detected at larger depths towards the west, whereas it is shallower towards the east. The opposite colour scales for the 410 km and 660 km depth maps were deliberately selected to visually represent the relationship between depth and temperature.

The general trend of a deeper 410 and a shallower 660 in the Canaries results in a thinner MTZ there at 216±2 km compared to 237±2 km around Madeira (Figures 6 d). These MTZ thickness values are derived from depth estimates of the 410 and 660 discontinuities, constrained to regions where observations for both discontinuities are available.

4.2 Sharpness and velocity contrast of detected discontinuities

Figure 7 shows the average amplitudes of the $P300s$, $P410s$, and $P660s$ phases relative to P across five frequency bands for both archipelagos. As expected for linear velocity gradients, the amplitude of all converted phases decreases with higher upper-frequency boundaries. We apply the criteria defined in section 3.5 to constrain the thickness of the discontinuities. In the Canary archipelago, $P300s$, $P410s$, and $P660s$ exhibit an amplitude reduction of ∼50% (w.r.t the lowest frequency band) at 0.64 Hz. Therefore, we consider $f^{max} = 0.64$ Hz for all converted phases, indicating that the detected discontinuities are sharp. Using Eq. 5 and corresponding values of v_p in ak135, we obtain $\Delta z_{300,Can} <$ 7 km, $\Delta z_{410,Can} < 7$ km, and $\Delta z_{660,Can} < 8$ km. In Madeira, $P300s$ exhibits an amplitude drop of ∼50% at 0.64 Hz, $P410s$ is still over 50% at 0.64 Hz. These results lead to sharp discontinuities: $\Delta z_{300,Mad} < 7$ km, $\Delta z_{410,Mad} < 7$ km (or even sharper). For $P660s$, the maximum frequency for which significant energy is converted is 0.48 Hz, which corresponds to $\Delta z_{660,Mad} < 11$ km.

In both archipelagos, the amplitude of $P300s$, $P410s$, and $P660s$ relative to P decreases gradually with increasing frequencies, shifting from average values of approxi-

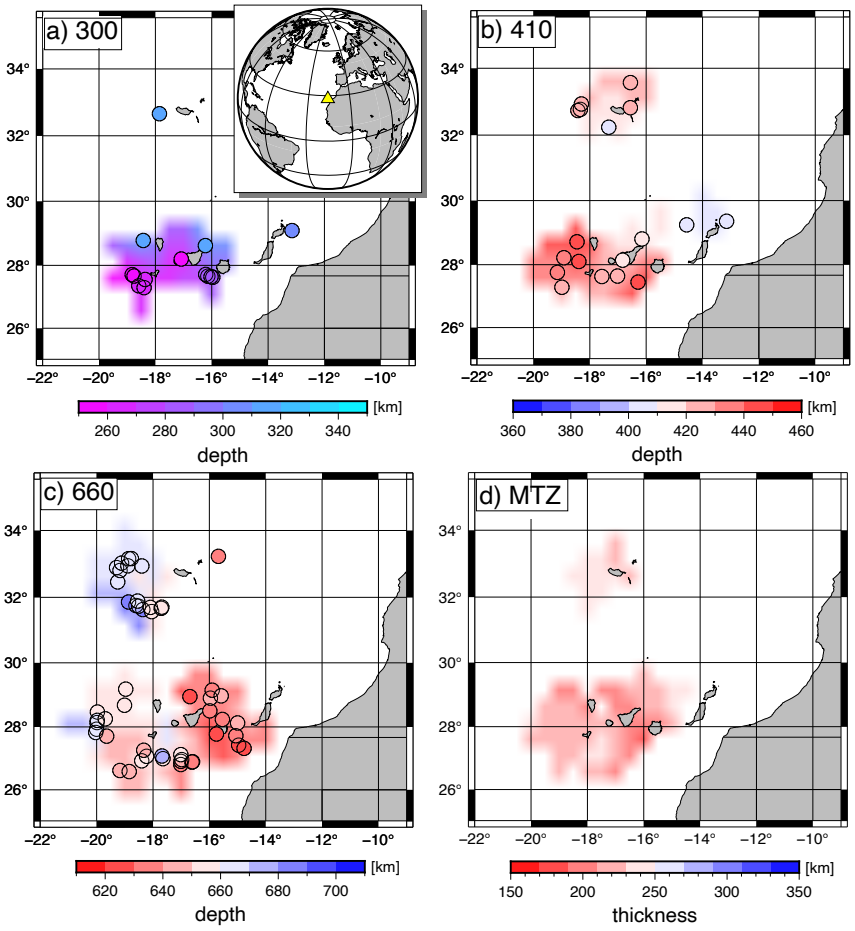

Figure 6. Maps showing discontinuity depth (a, b, c) and MTZ thickness surfaces (d), derived from depth estimates of the 410 and 660 discontinuities, constrained to regions where observations for both discontinuities are available. Circles with thicker lines correspond to robust detections in the PWS and LS, i.e., signals that satisfy the 95% confidence criteria. The ones with a thinner line correspond to robust detection only in the LS (the signal is visible in the PWS but it does not satisfy the 95% confidence criteria).

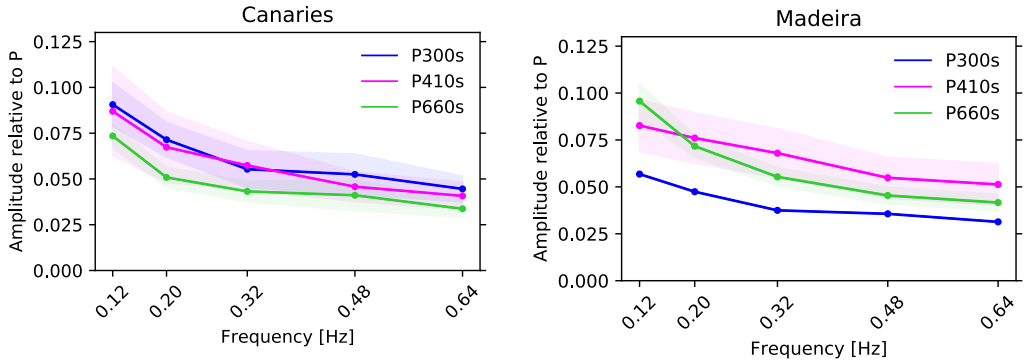

Figure 7. Change of relative amplitude of converted phases for different higher cut-off frequencies for the Canary (left) and Madeira (right) archipelagos. Values are given as a fraction of the initial P-phase amplitude. The shaded areas show uncertainties. Note, that $P300s$ in Madeira consists of only one measurement.

	phase	averaged observed amplitude ± 2 st err at 0.2 Hz	theoretical coefficients	v_S jump [%]	relative v_S jump 410/300	410/660
Madeira					1.6	1.1
	P300s	0.047± 0.012	0.047±0.001	5.1		
	P410s	0.076± 0.027	0.076±0.002	8.1		
	P660s	0.072± 0.012	0.072±0.002	7.6		
Canaries					0.96	1.3
	P300s	0.072± 0.017	0.071±0.002	7.6		
	P410s	0.067± 0.038	0.067±0.002	7.3		
	P660s	0.051± 0.011	0.051±0.002	5.5		

Table 1. Averaged observed amplitudes and theoretical coefficients used to constrain the velocity jumps (v_S jump) at target discontinuities. Theoretical coefficients are computed by averaging the transmission coefficients across a range of epicentral distances from 60° to 90°.

mately 0.09 to 0.04 (Figure 7). Amplitude variability is evident within individual bins across different frequencies, illustrating a consistent decreasing trend in amplitude (Figure S12). However, whereas the amplitude of $P300s$ is close to the amplitude of $P410s$ across all frequency bands in the Canaries (0.09±0.01 at 0.02-0.12 Hz to 0.04±0.01 at 0.02-0.64 Hz), it is the weakest around the Madeira archipelago (0.06±0.02 at 0.02-0.12 Hz to 0.03±0.01 at 0.02-0.64 Hz). This discrepancy is further emphasized by the fact that only one robust measurement of this discontinuity could be obtained there. Our observed relative amplitudes at 0.02-0.20 Hz for the Canary and Madeira archipelagos are displayed in Table 1. This specific frequency band was chosen because, at lower frequencies, the effects of the transmission coefficient response due to a velocity gradient on amplitudes are minimized. The table also shows the estimated velocity jumps and their corresponding theoretical transmission coefficients.

5 Discussion

5.1 Uncertainties in time observations

Uncertainties in our time detections are related to the smearing of the signal, which is attributed to several factors. First, it is related to the resolution in time, which is frequency-dependent. Moreover, additional complexities arise from random noise, the application of the linear move-out approximation, and the non-homogeneous distribution of epicentral distances. Each of these elements contributes to the smearing of signals in vespagrams. To assess and quantify time uncertainty in individual bins, we use the bootstrap method to estimate a time standard deviation for each detection. We found that on average the time uncertainty for the frequency band 0.02-0.2 Hz is 1.3+/-0.2 seconds. This corresponds to an average depth uncertainty of about 11+/-1 km. These values are not surprising when considering that seismic discontinuities are not strictly first-order discontinuities, as evidenced in the amplitude-frequency analysis. The thickness of the 410 and 660 discontinuities (typically on the order of 10 kilometers) imposes limitations on our time and depth resolution. Moreover, a velocity gradient in the Earth's upper mantle modulates seismic wave travel times across different frequencies (Helffrich & Bina, 1994; Bostock, 1999), with high-frequency converted waves experiencing more pronounced delays due to the gradual transition in wave speed (Bostock, 1999).

5.2 Robustness analysis of observed 420 and 660 topography

The absolute depth of discontinuities is determined by the velocity model used to correct the observed times. Incorrect determination of time corrections could lead to an inaccurate estimation of the depth of discontinuities. In Supporting material Section 3, we examine the time corrections and the depth correlations between the topography of the 410 and 660 discontinuities for both tomographic models, IBEM-P18/-S19 and MIT08, to assess the accuracy of our time-to-depth conversions. Based on this analysis, we conclude that MIT-P08 likely places the 410 and 660 discontinuities slightly deeper than their true depths. Conversely, the MTZ thickness remains unaffected by the mantle structure above it. The MTZ thickness is primarily influenced by the internal structure of the MTZ, characterized by smaller anomalies and consequently smaller errors. This is evident in Figure S14, showing similar time corrections for the $P410s$ and $P660s$.

5.3 Mantle transition zone in the Canary and Madeira archipelagos

5.3.1 Previous studies

A thinned MTZ has been found beneath the Canary and Madeira archipelagos in previous studies using RFs and SS/PP precursors. The effect is more pronounced ($\sim 15-20$ km thinner than the global average) beneath the Canaries (e.g., Li et al., 2003; Deuss, 2007; Gu et al., 2009; Martinez-Arevalo et al., 2013; Saki et al., 2015), but still evident beneath Madeira (e.g., Houser et al., 2008; Lawrence & Shearer, 2008; Deuss, 2009). There are different interpretations for the thinning of the MTZ. Whereas some studies explain those anomalies through the presence of hot mantle material, thus supporting the theory of existing plumes (e.g., Gu et al., 2009), other studies find that the thinning is similar to the widespread thinning of the MTZ beneath oceans observed from SS precursor studies; this thinning is not solely restricted to plumes (e.g., Li et al., 2003; Martinez-Arevalo et al., 2013).

The study of Civiero et al. (2021), based on results from high-resolution seismic tomography (Civiero et al., 2018; Civiero, Custódio, et al., 2019), shear-wave splitting (Schlaphorst et al., 2022) and gravity (Sandwell et al., 2014) along with plate reconstruction showed that the Madeira and Canary volcanism is fed by plume-like structures overlying the seismically slow Central-East Atlantic Anomaly (CEAA) developing as a dome-like instability beneath 700 km depth in connection to the African LLSVP. However, the two hotspot systems seem to be in different stages of development. While the Canary plume-like structure is still rooted in the CEAA, tomography results suggest that the Madeira plumelet is presently detached from it, extending from the surface down to at least 300 km depth (below which the resolution degrades), which was interpreted as a result of the Madeira plumelet being probably at a dying stage.

5.3.2 Our study

Our results support and reinforce the presence of a hot rising upwelling beneath the Canary Islands that extends through the MTZ in agreement with the interpretation of Civiero et al. (2021). We find that the MTZ is thinner in the Canary archipelago (Figure 6). This is attributed to a depressed 410 and an uplifted 660, which is consistent with the MTZ being crossed by a hot mantle upwelling. The negative correlation observed between the depths of the 410 and 660 discontinuities beneath the Canary Islands confirms that the polymorphs olivine and ringwoodite are the dominant minerals influencing the topography of both discontinuities.

In Madeira, the MTZ is also thinner, primarily due to a depressed 410 and a standard 660, suggesting that the thermal anomaly predominantly affects the 410 discontinuity. This is compatible with a low-velocity anomaly elongating downward to the top of the MTZ, i.e. extending more than 100 km deeper than the bulk of the anomaly im-

aged in the model by Civiero et al. (2021). The hypothesis of a possible deeper extension of the Madeira plumelet was admitted by the authors, based on considerations about the size of the anomaly and the coarser model resolution below this area. Our results provide complementary information that reinforces the hypothesis that the plumelet extends deeper than 300 km, but does not fully cross the MTZ beneath Madeira and is detached from the CEAA.

Additionally, we observe a lateral trend in the topography of discontinuities, which is more pronounced in the Canary archipelago. The 660 is shallower towards the east, while the 410 is deeper towards the west (Figure 6). Beneath Madeira, the 660 is shallower towards the east; however, this trend is less reliable here due to only one detection to the east of the archipelago. This lateral trend might indicate a lateral deflection of the plume. Numerical modelling of mantle flow highlights the potential role of edge-driven convection in the African craton in deflecting the mantle plume beneath the Canary archipelago towards the west (Negredo et al., 2022; Manjón-Cabeza Córdoba & Ballmer, 2022). While this scenario is plausible and compatible with Civiero's model, further study with expanded coverage of the study area using RFs is necessary to thoroughly test it.

By utilizing the Clapeyron slope of the olivine and ringwoodite PT, it becomes possible to estimate the total temperature variations across the MTZ beneath both archipelagos. If we substitute $\gamma_{660} = -2.0$ MPa/K, $\gamma_{410} = +4.00$ MPa/K and a reference MTZ thickness of 242 km from Lawrence and Shearer (2006) global RFs study in Eq. 4, the average MTZ thickness beneath the Canary archipelago (216 $\pm$ 2 km) translates to a temperature difference of $+144 \pm 11$ K. Similarly, the average MTZ thickness beneath the Madeira archipelago (237 ± 2 km) translates to a temperature difference of $+33 \pm 11$ K. These estimates provide insights into the thermal structure of the mantle anomalies beneath these volcanic regions. Excess temperatures within the mantle beneath these volcanic islands were independently confirmed using the chemical composition of the olivines, the liquidus phase of the alkaline magmas erupting on them (Putirka, 2008).

5.4 Evidences of thermochemical plume beneath the Canaries

The detection of PXs (also named $P300s$ throughout the article) serves as compelling evidence for the existence of chemical heterogeneities within the plume material.

5.4.1 The X discontinuity

The X discontinuity has been observed in a variety of tectonic environments: subduction zones (Zhang & Lay, 1993; Schmerr, 2015), stable continents (Wajeman, 1988; Pugh et al., 2023), several hotspots (Courtier et al., 2007; Bagley & Revenaugh, 2008; Schmerr, 2015; Kemp et al., 2019; Pugh et al., 2021, 2023), and ridges (Schmerr, 2015). However, it seems not to be omnipresent throughout the planet (e.g., Williams & Revenaugh, 2005; Schmerr et al., 2013). This suggests that such discontinuity is probably linked to some form of mantle heterogeneity(ies) promoting a specific PT. These observations over a broad range of possible mantle temperatures have led to several explanations for the X (summarized in Table S3). Out of the different mechanisms that have been proposed to explain the X discontinuity, the silica phase transition from coesite to stishovite has been suggested as the most plausible explanation for the X in hot mantle upwellings, such as the Canary archipelago, where it was previously observed (Pugh et al., 2021). The presence of this discontinuity implies the presence of polymorphic silica-rich phases beneath the study region at these depths. Within a plume setting, this material might correspond to recycled eclogite, more silica-rich than the dominant peridotite, aligning with thermochemical plume models (Kemp et al., 2019; Pugh et al., 2021, 2023).

The presence of eclogite beneath hotspots may be explained by bidirectional mass transfer in the dynamic Earth's interior, in agreement with a general model first proposed

by Hofmann and White (1982). The basaltic oceanic crust is recycled in the mantle through subduction, leading to the production of eclogitic rocks, denser than the dominant ultrabasic compositions (peridotites in the upper mantle) (Niu, 2018). This process contributes to the formation of chemical heterogeneities that gradually accumulate near the base of the lower mantle, forming what are known as slab graveyards (e.g., van der Meer et al., 2018; Jones et al., 2021). These heterogeneities partially explain the origin of LLSVPs (Koppers et al., 2021), which are located beneath Africa and the Pacific (e.g., French & Romanowicz, 2015). LLSVPs are believed to serve as nurseries for major deep-mantle-sourced hotspots like the Canary hotspot (Koppers et al., 2021). These upwellings, rooted in LLSVPs, transport recycled oceanic crust, including eclogite-type materials, to upper levels of the mantle (Hofmann & White, 1982; Tackley, 2000; Koppers et al., 2021). Owing to uranium enrichment of oceanic crust during sea-water alteration and lead depletion during subduction-induced dehydration, high $^{206}Pb/^{204}Pb$ is considered the best geochemical proxy for the presence in the mantle of ancient recycled oceanic crust, which is considered the cause for the HIMU mantle component (e.g., White, 2015). Here, the term HIMU refers to a mantle component characterized by a secular evolution under "High μ", where $\mu = U/Pb$; it is a typical geochemical signature found in some volcanic rocks, particularly those associated with hotspots and oceanic island basalts (OIBs). Lavas from both Canary (Gurenko et al., 2006, 2009; Day et al., 2010) and Madeira (e.g., Mata et al., 1998; Geldmacher & Hoernle, 2000; Gurenko et al., 2013) show evidence for the contribution of the HIMU mantle component, translated in moderately high $^{206}Pb/^{204}Pb$ (up to 20.270 and up to 19.989, respectively). These isotopic signatures independently support the geophysical evidence for the presence of eclogites in the mantle upwellings associated with those volcanic provinces. Recent numerical modelling indicates that mantle plumes can entrain about 20% basalt component as recycled eclogite, which leads to the formation of an eclogitic reservoir at depths of around 400 to 300 km (Ballmer et al., 2013; Dannberg & Sobolev, 2015). Since an eclogite proportion larger than 40% is required to seismically observe the X discontinuity (Schmerr, 2015; Kemp et al., 2019; Pugh et al., 2021), it has been suggested that with time the accumulation of eclogite above the MTZ would increase to the levels required to detect the PXs phase (Pugh et al., 2021).

The absence of a consistent PXs phase beneath Madeira suggests that, if a basalt reservoir is present, it likely contains less than 40% basalt. Conversely, localised detections of the PXs phase beneath Madeira and the Canaries can be interpreted as indications of localised accumulations of basalt.

Furthermore, it is plausible to hypothesise that the accumulation of the basalt reservoir beneath the Canary Islands is facilitated by the long-lasting and continuous hotspot feeding up to the present day. In contrast, if Madeira is in a declining phase, the accumulation of this reservoir may have been comparatively less efficient and/or may have already diminished after the downward retreat of the denser eclogite material, after the decrease of the plume positive buoyancy.

5.4.2 Compositional constraints from amplitude analysis

A mechanical mixture (MM) of basalt (MORB) and harzburgite, with basalt increasing with depth, accurately replicates the seismic data for realistic thermal structures of the upper mantle (Cammarano et al., 2009). First principle calculations indicate that the depth variations of the MTZ discontinuities are primarily influenced by temperature, whereas the magnitude of the corresponding velocity jumps is mainly affected by composition (e.g., Xu et al., 2008). Applying a simplified theoretical analysis to constrain the basalt proportion above the MTZ, we utilize the velocity contrast obtained in the amplitude analysis of the detected phases and the velocity contrast in a MM model of the mantle.

Theoretical velocity contrasts for the co→st, ol→wa and ri→br+mw phases are computed from the velocity models of Xu et al. (2008) for a potential temperature of 1800 K and basalt proportions ranging from 0% to 80%. Notably, the 410 discontinuity in these models aligns with the estimated depth beneath the Canaries, where a consistent PXs phase is detected. The predicted shear wave velocity jumps at depths of 300 km, 410 km, and 660 km, corresponding to the mentioned PT, are depicted in Figure 8 and summarized in the first four columns of Table 2. The analysis reveals that as the proportion of basalt increases, the velocity jumps for the 410 and 660 decrease, whereas the trend is opposite for the X discontinuity.

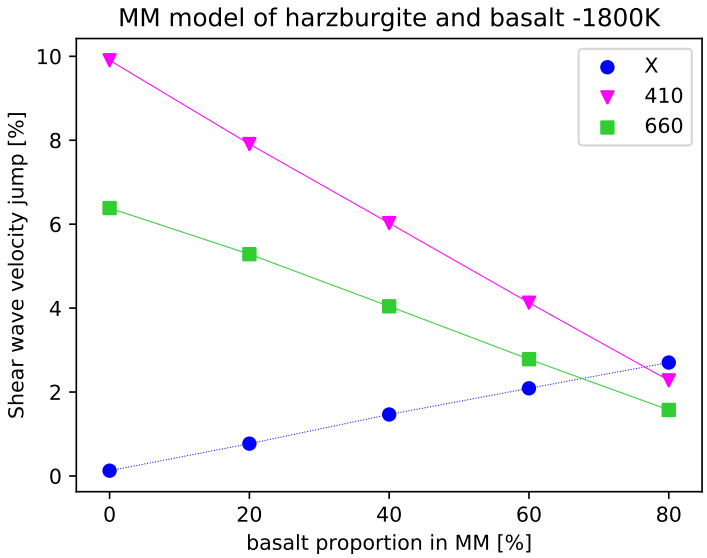

Figure 8. Predicted shear wave velocity jumps (in %) at depths of 300 km, 410 km, and 660 km, observed in a mechanical mixture (MM) of harzburgite and basalt with varying basalt proportions (f_b), obtained using the formula $V_{Sjump} = (v_2 - v_1)/2(v_1 + v_2)$, where v_1 and v_2 represent the velocities of the upper and lower layers, respectively.

basalt [%]	v_s jump [%]			relative v_S jump	
f_b	300	410	660	410/300	410/660
0	0.18	9.94	7.37	-	1.34
20	0.82	7.97	5.96	9.72	1.34
40	1.46	6.04	4.55	4.14	1.33
60	2.08	4.15	3.11	1.99	1.33
80	2.70	2.25	1.65	0.83	1.35

Table 2. Predicted shear wave velocity jumps at depths of 300 km, 410 km, and 660 km, observed in a mechanical mixture of harzburgite and basalt with varying proportions of basalt, f_b and a potential temperature of 1800 K. The last two columns display the relative velocity jumps between 410 and 300, and 410 and 660 as the proportion of basalt increases.

Our estimated velocity jumps (column four in Table 1) are obtained from the amplitude analysis of detected converted phases. These phases can be difficult to detect on

individual RFs as arrivals are often relatively weak and close to the noise level. Occasionally, some phases show anomalously large amplitudes, in which case they can be identified individually. Generally, these signals are most reliably detected when a large number of RFs from small CCP areas are stacked but even then converted phases can be weak, thus making it challenging to robustly identify them. For example, for $P300s$, we only obtained 18 robust detections out of 34 good-quality CCP stacks. Moreover, the amplitude of converted phases in stacked RFs exhibits variability due to factors such as noise, focusing, and defocusing by small-scale topography variations. Consequently, constraints on absolute velocity jumps based on these amplitudes may not be accurate. Therefore, rather than interpreting the absolute values of velocity jumps, we focus on the relative values of the estimated velocity jumps (last two columns of Table 1). The corresponding theoretical values (relative velocity jumps w.r.t the 410) for varying proportions of basalt are displayed in the last two columns of Table 2. This theoretical analysis reveals that the relative velocity jump between the 410 and 660 remains relatively constant for varying fractions of basalt. However, the relative velocity jump between the 410 and X decreases as the proportion of basalt increases. In other words, the strength of the X discontinuity becomes more prominent for higher values of f_b, while the opposite trend is observed for the 410 and 660 discontinuities.

Our estimations for the relative velocity jumps between the 410 and X are 0.96 and 1.6 (Table 1), for the Canary and Madeira archipelagos, respectively. These values correspond to a proportion of basalt between 60% and 80% (Table 2). Based on the reliability of the X discontinuity in the Canaries dataset, we conclude that the accumulation of basalt is more significant there. For Madeira, the accumulation of basalt appears to be very localized.

6 Conclusions

Using P RFs, we conduct a systematic regional study to map out mantle seismic discontinuities beneath the Madeira and Canary archipelagos. We identify converted phases beneath both archipelagos for transition zone discontinuities, namely the 410 and 660. In the Canary Islands, the 410 is deeper (428 ± 4 km) and the 660 is shallower (647 ± 2 km). The MTZ is thinner (216 ± 2 km) compared to the global average suggesting the presence of a hot mantle upwelling characterised by excess temperatures that we estimate of $+144 \pm 11$ K with respect to the surrounding mantle. Furthermore, the dominant minerals influencing the topography of the 410 and 660 are, respectively, olivine and its polymorph ringwoodite. The discontinuity sharpness analysis provides additional support to this conclusion, as it reveals clear and well-defined 660 discontinuity features, which is in contrast to a broad 660 that would arise due to garnet being the dominant mineral. Beneath Madeira, the 660 discontinuity is close to the reference value and the 410 discontinuity is found at greater depths (421 ± 3 km). Here the MTZ is cooler than below the Canaries, with estimated excess temperatures of only $+33 \pm 11$ K with respect to the surrounding mantle. Furthermore, beneath the Canaries, we have reliable detections of the X discontinuity, attributed to the coesite-to-stishovite PT in regions of the upper mantle enriched in eclogite (as expected for thermochemical plumes). The X discontinuity is in the range of 251-316 km depth in a broad area beneath the Canaries, but it is observed at only one isolated location beneath Madeira at 313 km. We estimate that the basalt proportion in the plume, between 300-400 km, is 60-80%, with accumulation being more significant in the Canaries than in Madeira. The MTZ thickness, the presence of the X discontinuity, and the high basalt fraction provide compelling evidence for a deep-seated thermochemical plume beneath the study area, which feeds an active upwelling that presently crosses the MTZ beneath the Canaries. Beneath Madeira, it appears that only the upper portion of the MTZ is slightly affected. This suggests that the upwelling in this area might be less vigorous or currently disconnected from its deeper

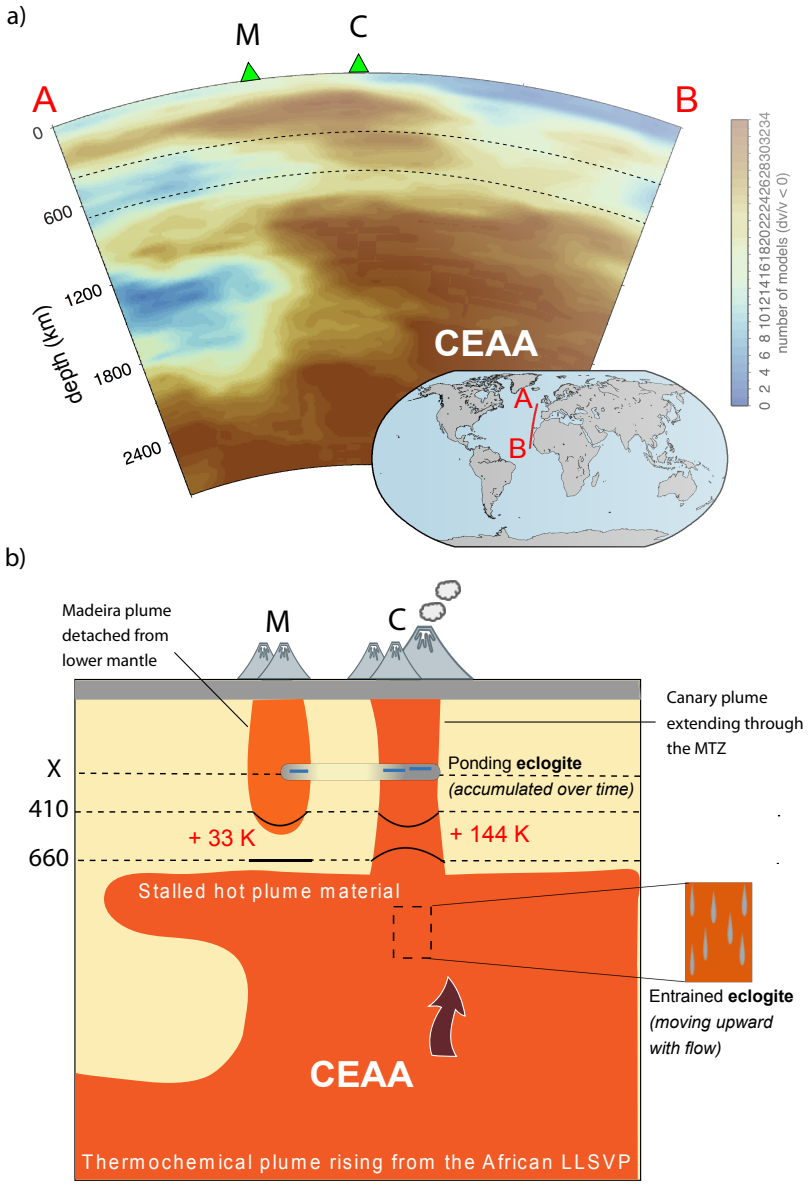

Figure 9. a) Vote cross-section created with the SubMachine tool (http://www.earth.ox.ac.uk/ smachine/) using 34 P- and S-wave tomographic models and illustrating the most robust long-wavelength low-velocity anomalies in the mantle beneath Canaries (C) and Madeira (M). b) Cartoon illustrating the Canary Plume's extension through the upper mantle and the detached Madeira upwelling, incorporating constraints from our analysis (X discontinuity, eclogite above the MTZ, topography of MTZ discontinuities and temperature of MTZ).

source. This interpretation is in line with tomographic images. We have summarized our findings in the conceptual model presented in Figure 9.

Open Research Section

Data from IPMA permanent stations (PM) are available from IPMA at `http://ceida.ipma.pt`. Data from DOCTAR experiment (Y7) are available on request from the GFZ at `https://dataservices.gfz-potsdam.de/portal/`. Data from the Global Seismograph Network (IU) are available from the IRIS Data Management Center (IRIS-DMC): `http://service.iris.edu/fdsnws/dataselect/1/`. Data from the Spanish Digital Seismic Network (ES) are available on request from the Institut Cartogràfic i Geològic de Catalunya (ICGC): `http://ws.icgc.cat/fdsnws/dataselect/1/`.
DOI information or FDSN network information, where available, are:
IU: `https://doi.org/10.7914/SN/IU`
ES: `https://10.7914/SN/ES`
Y7: `https://www.fdsn.org/networks/detail/Y7_2011/`

Acknowledgments
We thank the associate editor and two anonymous reviewers for thoughtful comments and suggestions that helped improving the paper. This work is a contribution to projects SIGHT (Ref. PTDC/CTA-GEF/30264/2017) and GEMMA (PTDC/CTA-GEO/2083/2021). This work was also supported by the Portuguese Fundação para a Ciência e a Tecnologia (FCT) I.P./MCTES through national funds (PIDDAC) – UIDB/50019/2020. LB would like to express sincere gratitude to the University of La Serena's Research Incentive Program for Academics (PIA) for their generous support.

References

Aki, K., & Richards, P. (2002). *Quantitative Seismology.* University Science Books.

Allègre, C. J., & Turcotte, D. L. (1986). Implications of a two-component marble-cake mantle. , *323*(6084), 123-127. doi: 10.1038/323123a0

Ammon, C. J. (1991). The isolation of receiver effects from teleseismic P waveforms. *Bull. Seism. Soc. Am.*, *81*(6), 2504-2510. doi: 10.1785/BSSA0810062504

Bagley, B., & Revenaugh, J. (2008). Upper mantle seismic shear discontinuities of the Pacific. *Journal of Geophysical Research: Solid Earth*, *113*(B12). doi: 10.1029/2008JB005692

Ballmer, M. D., Ito, G., Wolfe, C. J., & Solomon, S. C. (2013). Double layering of a thermochemical plume in the upper mantle beneath Hawaii. *Earth and Planetary Science Letters*, *376*, 155–164. doi: 10.1016/j.epsl.2013.06.022

Bina, C. R., & Helffrich, G. (1994). Phase transition Clapeyron slopes and transition zone seismic discontinuity topography. *Journal of Geophysical Research*, *99*(B8), 15853-15860. doi: 10.1029/94JB00462

Bonatto, L., Piromallo, C., & Cottaar, S. (2020). The Transition Zone Beneath West Argentina-Central Chile Using P-to-S Converted Waves. *Journal of Geophysical Research: Solid Earth*, *125*(8), e2020JB019446. doi: 10.1029/2020JB019446

Bonatto, L., Schimmel, M., Gallart, J., & Morales, J. (2015). The upper-mantle transition zone beneath the Ibero-Maghrebian region as seen by teleseismic *Pds* phases . *Tectonophysics*, *663*, 212 - 224. (Special issue on Iberia geodynamics: An integrative approach from the Topo-Iberia framework) doi: 10.1016/j.tecto.2015.02.002

Bostock, M. G. (1999). Seismic waves converted from velocity gradient anomalies in the Earth's upper mantle. *Geophys. J. Int.*, *138*(3), 747-756. doi: 10.1046/j.1365-246X.1999.00902.x

Cammarano, F., Romanowicz, B., Stixrude, L., Lithgow-Bertelloni, C., & Xu, W. (2009). Inferring the thermochemical structure of the upper mantle from seismic data. *Geophysical Journal International*, *179*(2), 1169-1185. doi: 10.1111/j.1365-246X.2009.04338.x

Carracedo, J. C., & Troll, V. R. (2021). North-East Atlantic Islands: The Macaronesian Archipelagos. In D. Alderton & S. A. Elias (Eds.), *Encyclopedia of geology (second edition)* (Second Edition ed., p. 674-699). Oxford: Academic Press. doi: 10.1016/B978-0-08-102908-4.00027-8

Civiero, C., Armitage, J. J., Goes, S., & Hammond, J. O. S. (2019). The Seismic Signature of Upper-Mantle Plumes: Application to the Northern East African Rift. *Geochemistry, Geophysics, Geosystems*, *20*(12), 6106-6122. doi: 10.1029/2019GC008636

Civiero, C., Custódio, S., Neres, M., Schlaphorst, D., Mata, J., & Silveira, G. (2021). The Role of the Seismically Slow Central-East Atlantic Anomaly in the Genesis of the Canary and Madeira Volcanic Provinces. *Geophysical Research Letters*, *48*(13), e92874. doi: 10.1029/2021GL092874

Civiero, C., Custódio, S., Rawlinson, N., Strak, V., Silveira, G., Arroucau, P., & Corela, C. (2019). Thermal Nature of Mantle Upwellings Below the Ibero-Western Maghreb Region Inferred From Teleseismic Tomography. *Journal of Geophysical Research: Solid Earth*, *124*(2), 1781-1801. doi: 10.1029/2018JB016531

Civiero, C., Strak, V., Custódio, S., Silveira, G., Rawlinson, N., Arroucau, P., & Corela, C. (2018). A common deep source for upper-mantle upwellings below the Ibero-western Maghreb region from teleseismic P-wave traveltime tomography. *Earth and Planetary Science Letters*, *499*, 157-172. doi: 10.1016/j.epsl.2018.07.024

Collier, J. D., & Helffrich, G. R. (2001). The thermal influence of the subducting slab beneath South America from 410 and 660 km discontinuity observations. *Geophys. J. Int.*, *147*(2), 319-329. doi: 10.1046/j.1365-246X.2001.00532.x

Courtier, A. M., Bagley, B., & Revenaugh, J. (2007). Whole mantle discontinuity structure beneath Hawaii. *Geophysical Research Letters*, *34*(17). doi: 10.1029/2007GL031006

Crotwell, H. P., Owens, T. J., & Ritsema, J. (1999). The TauP Toolkit: Flexible seismic travel-time and ray-path utilities. *Seismological Research Letters*, *70*, 154-160. doi: 10.1785/gssrl.70.2.154

Dannberg, J., & Sobolev, S. V. (2015). Low-buoyancy thermochemical plumes resolve controversy of classical mantle plume concept. *Nature communications*, *6*(1), 1–9. doi: 10.1038/ncomms7960

Day, J. M. D., Pearson, D. G., Macpherson, C. G., Lowry, D., & Carracedo, J. C. (2010). Evidence for distinct proportions of subducted oceanic crust and lithosphere in HIMU-type mantle beneath El Hierro and La Palma, Canary Islands. *Geochimica et Cosmochimica Acta*, *74*(22), 6565-6589. doi: 10.1016/j.gca.2010.08.021

Deuss, A. (2007). Seismic observations of transition-zone discontinuities beneath hotspot locations. *Special Paper 430: Plates, Plumes and Planetary Processes*, 121-136. doi: 10.1130/2007.2430(07)

Deuss, A. (2009). Global Observations of Mantle Discontinuities Using SS and PP Precursors. *Surveys in Geophysics*, *30*(4-5), 301-326. doi: 10.1007/s10712-009-9078-y

Deuss, A., Redfern, S. A. T., Chambers, K., & Woodhouse, J. H. (2006). The Nature of the 660-Kilometer Discontinuity in Earth's Mantle from Global Seismic Observations of PP Precursors. *Science*, *311*(5758), 198-201. doi: 10.1126/science.1120020

Dziewonski, A. M., & Anderson, D. L. (1981). Preliminary reference Earth model. *Physics of the Earth and Planetary Interiors*, *25*(4), 297 - 356. doi: 10.1016/

0031-9201(81)90046-7

French, S., & Romanowicz, B. (2015). Broad plumes rooted at the base of the Earth's mantle beneath major hotspots. *Nature*, *525*, 95-99. doi: 10.1038/nature14876

Geldmacher, J., & Hoernle, K. (2000). The 72 Ma geochemical evolution of the Madeira hotspot (eastern North Atlantic): recycling of Paleozoic (500 Ma) oceanic lithosphere. *Earth and Planetary Science Letters*, *183*(1), 73-92. doi: 10.1016/S0012-821X(00)00266-1

Geldmacher, J., Hoernle, K., Bogaard, P., Duggen, S., & Werner, R. (2005). New 40Ar/39Ar age and geochemical data from seamounts in the Canary and Madeira volcanic provinces: Support for the mantle plume hypothesis. *Earth and Planetary Science Letters*, *237*(1), 85-101. doi: 10.1016/j.epsl.2005.04.037

Geldmacher, J., Hoernle, K., van den Bogaard, P., Zankl, G., & Garbe-Schönberg, D. (2001). Earlier history of the 70-Ma-old Canary hotspot based on the temporal and geochemical evolution of the Selvagen Archipelago and neighboring seamounts in the eastern North Atlantic. *Journal of Volcanology and Geothermal Research*, *111*(1), 55-87. doi: 10.1016/S0377-0273(01)00220-7

Gu, Y. J., An, Y., Sacchi, M., Schultz, R., & Ritsema, J. (2009). Mantle reflectivity structure beneath oceanic hotspots. *Geophysical Journal International*, *178*(3), 1456-1472. doi: 10.1111/j.1365-246X.2009.04242.x

Gurenko, A. A., Geldmacher, J., Hoernle, K. A., & Sobolev, A. V. (2013). A composite, isotopically-depleted peridotite and enriched pyroxenite source for Madeira magmas: Insights from olivine. *Lithos*, *170*, 224-238. doi: 10.1016/j.lithos.2013.03.002

Gurenko, A. A., Hoernle, K. A., Hauff, F., Schmincke, H. U., Han, D., Miura, Y. N., & Kaneoka, I. (2006). Major, trace element and Nd-Sr-Pb-O-He-Ar isotope signatures of shield stage lavas from the central and western Canary Islands: Insights into mantle and crustal processes. *Chemical Geology*, *233*(1-2), 75-112. doi: 10.1016/j.chemgeo.2006.02.016

Gurenko, A. A., Sobolev, A. V., Hoernle, K. A., Hauff, F., & Schmincke, H.-U. (2009). Enriched, HIMU-type peridotite and depleted recycled pyroxenite in the Canary plume: A mixed-up mantle. *Earth and Planetary Science Letters*, *277*(3-4), 514-524. doi: 10.1016/j.epsl.2008.11.013

Helffrich, G. (2000). Topography of the transition zone seismic discontinuities. *Reviews of Geophysics*, *38*(1), 141-158. doi: 10.1029/1999RG000060

Helffrich, G., & Bina, C. R. (1994). Frequency dependence of the visibility and depths of mantle seismic discontinuities. *Geophysical Research Letters*, *21*(24), 2613-2616. doi: https://doi.org/10.1029/94GL02341

Helffrich, G. R., & Wood, B. J. (2001). The Earth's mantle. , *412*(6846), 501-507. doi: https://doi.org/10.1038/35087500

Hirose, K. (2002). Phase transitions in pyrolitic mantle around 670-km depth: Implications for upwelling of plumes from the lower mantle. *Journal of Geophysical Research: Solid Earth*, *107*(B4), ECV 3-1-ECV 3-13. doi: https://doi.org/10.1029/2001JB000597

Hofmann, A. W., & White, W. M. (1982). Mantle plumes from ancient oceanic crust. *Earth and Planetary Science Letters*, *57*(2), 421-436. doi: 10.1016/0012-821X(82)90161-3

Houser, C., Masters, G., Flanagan, M., & Shearer, P. (2008). Determination and analysis of long-wavelength transition zone structure using SS precursors. *Geophysical Journal International*, *174*(1), 178-194. doi: 10.1111/j.1365-246X.2008.03719.x

Instituto Português do Mar e da Atmosfera, I.P. (2006). *Portuguese National Seismic Network.* International Federation of Digital Seismograph Networks. Retrieved from `https://www.fdsn.org/networks/detail/PM/` doi:

10.7914/SN/PM

Jenkins, J., Deuss, A., & Cottaar, S. (2017). Converted phases from sharp 1000 km depth mid-mantle heterogeneity beneath Western Europe. *Earth and Planetary Science Letters*, *459*, 196-207. doi: 10.1016/j.epsl.2016.11.031

Jones, T. D., Sime, N., & van Keken, P. E. (2021). Burying Earth's Primitive Mantle in the Slab Graveyard. *Geochemistry, Geophysics, Geosystems*, *22*(3), e2020GC009396. doi: 10.1029/2020GC009396

Juliá, J. (2007). Constraining velocity and density contrasts across the crust—mantle boundary with receiver function amplitudes. *Geophys. J. Int.*, *171*(1), 286-301. doi: 10.1111/j.1365-2966.2007.03502.x

Kemp, M., Jenkins, J., Maclennan, J., & Cottaar, S. (2019). X-discontinuity and transition zone structure beneath Hawaii suggests a heterogeneous plume. *Earth and Planetary Science Letters*, *527*, 115781. doi: 10.1016/j.epsl.2019.115781

Koppers, A. A. P., Becker, T. W., Jackson, M. G., Konrad, K., Müller, R. D., Romanowicz, B., ... Whittaker, J. M. (2021). Mantle plumes and their role in Earth processes. *Nat Rev Earth Environ*, *2*, 382–401. doi: 10.1038/s43017-021-00168-6

Langston, C. A. (1979). Structure under Mount Rainier, Washington, inferred from teleseismic body waves. *J. Geophys. Res.*, *84*(B9), 4749-4762. doi: 10.1029/JB084iB09p04749

Lawrence, J. F., & Shearer, P. M. (2006). A global study of transition zone thickness using receiver functions. *Journal of Geophysical Research: Solid Earth*, *111*(B6). doi: 10.1029/2005JB003973

Lawrence, J. F., & Shearer, P. M. (2008). Imaging mantle transition zone thickness with SdS-SS finite-frequency sensitivity kernels. *Geophysical Journal International*, *174*(1), 143-158. doi: 10.1111/j.1365-246X.2007.03673.x

Li, C., van der Hilst, R. D., Engdahl, E. R., & Burdick, S. (2008). A new global model for P wave speed variations in Earth's mantle. *Geochemistry, Geophysics, Geosystems*, *9*(5). (Q05018) doi: 10.1029/2007GC001806

Li, X., Kind, R., & Yuan, X. (2003). Seismic study of upper mantle and transition zone beneath hotspots. *Physics of the Earth and Planetary Interiors*, *136*(1-2), 79-92. doi: 10.1016/S0031-9201(03)00021-9

Liu, H., Wang, W., Jia, X., Leng, W., Wu, Z., & Sun, D. (2018, August). The combined effects of post-spinel and post-garnet phase transitions on mantle plume dynamics. *Earth and Planetary Science Letters*, *496*, 80-88. doi: 10.1016/j.epsl.2018.05.031

Manjón-Cabeza Córdoba, A., & Ballmer, M. D. (2022). The role of edge-driven convection in the generation of volcanism – Part 2: Interaction with mantle plumes, applied to the Canary Islands. *Solid Earth*, *13*(10), 1585–1605. doi: 10.5194/se-13-1585-2022

Martinez-Arevalo, C., Mancilla, F. d. L., Helffrich, G., & Garcia, A. (2013). Seismic evidence of a regional sublithospheric low velocity layer beneath the Canary Islands. *Tectonophysics*, *608*, 586-599. doi: 10.1016/j.tecto.2013.08.021

Mata, J., Kerrich, R., MacRae, N. D., & Wu, T. W. (1998). Elemental and isotopic (Sr, Nd, and Pb) characteristics of Madeira Island basalts: evidence for a composite HIMU - EM I plume fertilizing lithosphere. *Canadian Journal of Earth Sciences*, *35*(9), 980-997. doi: 10.1139/e98-046

Matos, C., Silveira, G., Matias, L., Caldeira, R., Ribeiro, M. L., Dias, N. A., ... Bento dos Santos, T. (2015). Upper crustal structure of madeira island revealed from ambient noise tomography. *Journal of Volcanology and Geothermal Research*, *298*, 136-145. doi: 10.1016/j.jvolgeores.2015.03.017

Morgan, W. J. (1972). Plate Motions and Deep Mantle Convection. In *Studies in Earth and Space Sciences.* Geological Society of America. doi: 10.1130/MEM132-p7

Negredo, A. M., van Hunen, J., Rodríguez-González, J., & Fullea, J. (2022). On the origin of the Canary Islands: Insights from mantle convection modelling. *Earth and Planetary Science Letters*, *584*, 117506. doi: https://doi.org/10.1016/j.epsl.2022.117506

Niu, Y. (2018). Origin of the LLSVPs at the base of the mantle is a consequence of plate tectonics – A petrological and geochemical perspective. *Geoscience Frontiers*, *9*(5), 1265-1278. (SPECIAL ISSUE: Frontiers in geoscience:A tribute to Prof. Xuanxue Mo) doi: https://doi.org/10.1016/j.gsf.2018.03.005

Paulssen, H. (1988). Evidence for a Sharp 670-km Discontinuity as Inferred From P-to-s Converted Waves. *J. Geophys. Res.*, *93*(B9), 10489-10500. doi: 10.1029/JB093iB09p10489

Phinney, R. (1964). Structure of the Earth's Crust from Spectral Behavior of Long–Period Body Waves. *J. Geophys. Res.*, *69*(14), 2997-3017. doi: 10.1029/JZ069i014p02997

Pugh, S., Boyce, A., Bastow, I. D., Ebinger, C. J., & Cottaar, S. (2023). Multigenetic Origin of the X-Discontinuity Below Continents: Insights From African Receiver Functions. *Geochemistry, Geophysics, Geosystems*, *24*(3), e2022GC010782. doi: 10.1029/2022GC010782

Pugh, S., Jenkins, J., Boyce, A., & Cottaar, S. (2021). Global receiver function observations of the X-discontinuity reveal recycled basalt beneath hotspots. *Earth and Planetary Science Letters*, *561*, 116813. doi: 10.1016/j.epsl.2021.116813

Putirka, K. (2008). Excess temperatures at ocean islands: Implications for mantle layering and convection. *Geology*, *36*(4), 283-286. doi: 10.1130/G24615A.1

Richards, P. (1972). Seismic waves reflected from velocity gradient anomalies within the Earth's upper mantle. *J. Geophys. Res.*, *38*, 517-527. doi: 10.1046/j.1365-246x.1999.00902.x

Ritsema, J., & Van Heijst, H. J. (2002). Constraints on the correlation of P- and S-wave velocity heterogeneity in the mantle from P, PP, PPP and PKPab travel times. *Geophys. J. Int.*, *149*(2), 482-489. doi: 10.1046/j.1365-246X.2002.01631.x

Saki, M., Thomas, C., Nippress, S. E. J., & Lessing, S. (2015). Topography of upper mantle seismic discontinuities beneath the North Atlantic: The Azores, Canary and Cape Verde plumes. *Earth and Planetary Science Letters*, *409*, 193-202. doi: 10.1016/j.epsl.2014.10.052

Sandwell, D. T., Müller, R. D., Smith, W. H. F., Garcia, E., & Francis, R. (2014). New global marine gravity model from CryoSat-2 and Jason-1 reveals buried tectonic structure. *Science*, *346*(6205), 65-67. doi: 10.1126/science.1258213

Schimmel, M., & Paulssen, H. (1997). Noise reduction and detection of weak, coherent signals through phase-weighted stacks. *Geophys. J. Int.*, *130*(2), 497-505. doi: 10.1111/j.1365-246X.1997.tb05664.x

Schlaphorst, D., Silveira, G., Mata, J., Krüger, F., Dahm, T., & Ferreira, A. M. G. (2022). Heterogeneous seismic anisotropy beneath Madeira and Canary archipelagos revealed by local and teleseismic shear wave splitting. *Geophysical Journal International*, *233*(1), 510-528. doi: 10.1093/gji/ggac472

Schmerr, N. (2015). Imaging mantle heterogeneity with upper mantle seismic discontinuities. In A. Khan & F. Deschamps (Eds.), *The earth's heterogeneous mantle: A geophysical, geodynamical, and geochemical perspective* (pp. 79–104). Cham: Springer International Publishing. doi: 10.1007/978-3-319-15627-9_3

Schmerr, N. C., Kelly, B. M., & Thorne, M. S. (2013). Broadband array observations of the 300 km seismic discontinuity. *Geophysical Research Letters*, *40*(5), 841-846. doi: 10.1002/grl.50257

Shearer, P. M., & Flanagan, M. P. (1999). Seismic Velocity and Density Jumps Across the 410- and 660-Kilometer Discontinuities. *Science*, *285*, 1545-1548. doi: 10.1126/science.285.5433.1545

Tackley, P. J. (2000). Mantle Convection and Plate Tectonics: Toward an Integrated Physical and Chemical Theory. *Science*, *288*(5473), 2002-2007. doi: 10.1126/science.288.5473.2002

van der Meer, D. G., van Hinsbergen, D. J., & Spakman, W. (2018). Atlas of the underworld: Slab remnants in the mantle, their sinking history, and a new outlook on lower mantle viscosity. *Tectonophysics*, *723*, 309-448. doi: https://doi.org/10.1016/j.tecto.2017.10.004

van der Meijde, M., Marone, F., Giardini, D., & van der Lee, S. (2003). Seismic Evidence for Water Deep in Earth's Upper Mantle. *Science*, *300*(5625), 1556-1558. doi: 10.1126/science.1083636

Vidale, J. E., & Benz, H. M. (1992). Upper-mantle seismic discontinuities and the thermal structure of subduction zones. *Nature*, *356*(6371), 678-683. doi: 10.1038/356678a0

Vinnik, L. (1977). Detection of waves converted from P to SV in the mantle. *J. Phys. Earth Planet. Inter.*, *15*(1), 39-45. doi: 10.1016/0031-9201(77)90008-5

Wajeman, N. (1988). Detection of underside P reflections at mantle discontinuities by stacking broadband data. *Geophysical Research Letters*, *15*(7), 669-672. doi: 10.1029/GL015i007p00669

Weidner, D. J., & Wang, Y. (1998). Chemical- and Clapeyron-induced buoyancy at the 660 km discontinuity. *Journal of Geophysical Research: Solid Earth*, *103*(B4), 7431-7441. doi: 10.1029/97JB03511

White, W. M. (2015). Isotopes, DUPAL, LLSVPs, and Anekantavada. *Chemical Geology*, *419*, 10-28. doi: 10.1016/j.chemgeo.2015.09.026

Williams, Q., & Revenaugh, J. (2005). Ancient subduction, mantle eclogite, and the 300 km seismic discontinuity. *Geology*, *33*(1), 1-4. doi: 10.1130/G20968.1

Xu, W., Lithgow-Bertelloni, C., Stixrude, L., & Ritsema, J. (2008). The effect of bulk composition and temperature on mantle seismic structure. *Earth and Planetary Science Letters*, *275*(1), 70 - 79. doi: 10.1016/j.epsl.2008.08.012

Yu, Y. G., Wentzcovitch, R. M., Vinograd, V. L., & Angel, R. J. (2011). Thermodynamic properties of $MgSiO_3$ majorite and phase transitions near 660 km depth in $MgSiO_3$ and Mg_2SiO_4: A first principles study. *Journal of Geophysical Research: Solid Earth*, *116*(B2), B02208. doi: 10.1029/2010JB007912

Zhang, Z., & Lay, T. (1993). Investigation of upper mantle discontinuities near Northwestern Pacific Subduction Zones using precursors to sSH. *Journal of Geophysical Research: Solid Earth*, *98*(B3), 4389-4405. doi: 10.1029/92JB02050

Ziberna, L., Klemme, S., & Nimis, P. (2013). Garnet and spinel in fertile and depleted mantle: insights from thermodynamic modelling. *Contributions to Mineralogy and Petrology*, *166*(2), 411-421. doi: 10.1007/s00410-013-0882-5

References from the Supporting Information

Akaogi, M., Takayama, H., Kojitani, H., Kawaji, H., & Atake, T. (2007). Low-temperature heat capacities, entropies and enthalpies of Mg_2SiO_4 polymorphs, and α - β - γ and post-spinel phase relations at high pressure. *Phys Chem Minerals, 34*, 169–183, doi: 10.1007/s00269-006-0137-3

Akaogi, M., & Akimoto, S.-I. (1980). High-pressure stability of a dense hydrous magnesian silicate $Mg_{23}Si_8O_{42}H_6$ and some geophysical implications. *Journal of Geophysical Research: Solid Earth, 85* (B12), 6944–6948, doi: 10.1029/JB085iB12p06944

Allen, R. V. (1978). Automatic earthquake recognition and timing from single traces. *Bulletin of the Seismological Society of America, 68* (5), 1521–1532, doi:10.1785/BSSA0680051521

Bonatto, L., Schimmel, M., Gallart, J., & Morales, J. (2015). The upper-mantle transition zone beneath the Ibero-Maghrebian region as seen by teleseis-

mic Pds phases [Special issue on Iberia geodynamics: An integrative approach from the Topo-Iberia framework]. *Tectonophysics, 663*, 212–224, doi:10.1016/j.tecto.2015.02.002

Bonatto, L., Piromallo, C., & Cottaar, S. (2020). The Transition Zone Beneath West Argentina-Central Chile Using P-to-S Converted Waves. *Journal of Geophysical Research: Solid Earth, 125* (8), e2020JB019446, doi:10.1029/2020JB019446

Boyce, A., & Cottaar, S. (2021). Insights Into Deep Mantle Thermochemical Contributions to African Magmatism From Converted Seismic Phases. Geochemistry, *Geophysics, Geosystems, 22* (3), Article e2020GC009478, e2020GC009478, doi:10.1029/2020GC009478

Chen, T., Gwanmesia, G. D., Wang, X., Zou, Y., Liebermann, R. C., Michaut, C., & Li, B. (2015). Anomalous elastic properties of coesite at high pressure and implications for the upper mantle X-discontinuity. *Earth and Planetary Science Letters, 412*, 42–51, doi:10.1016/j.epsl.2014.12.025

Clayton, R. W., & Wiggins, R. A. (1976). Source shape estimation and deconvolution of teleseismic body waves. *J. R. Astr. Soc., 47* (1), 151–177, doi:10.1111/j.1365-246X.1976.tb01267.x

Dueker, K. G., & Sheehan, A. F. (1998). Mantle discontinuity structure beneath the Colorado Rocky Mountains and High Plains. *Journal of Geophysical Research: Solid Earth, 103* (B4), 7153–7169, doi:10.1029/97JB03509

Ganguly, J., & Frost, D. J. (2006). Stability of anhydrous phase B: Experimental studies and implications for phase relations in subducting slab and the X discontinuity in the mantle. *Journal of Geophysical Research: Solid Earth, 111* (B6), doi:10.1029/2005JB003910

Katsura, T., Yamada, H., Nishikawa, O., Song, M., Kubo, A., Shinmei, T., Yokoshi, S., Aizawa, Y., Yoshino, T., Walter, M. J., & Ito, E. (2004). Olivine-wadsleyite transition in the system $(Mg,Fe)_2SiO_4$. J. *Geophys. Res., 109, B02209*, doi:10.1029/2003JB002438

Kemp, M., Jenkins, J., Maclennan, J., & Cottaar, S. (2019). X-discontinuity and transition zone structure beneath Hawaii suggests a heterogeneous plume. *Earth and Planetary Science Letters, 527*, 115781, doi:10.1016/j.epsl.2019.115781

Litasov, K. D., Ohtani, E., Sano, A., Suzuki, A., & Funakoshi, K. (2005). Wet subduction versus cold subduction. *Geophysical Research Letters, 32* (13), doi:10.1029/2005GL022921

Liu, J., Topor, L., Zhang, J., Navrotsky, A., & Liebermann, R. C. (1996). Calorimetric study of the coesite-stishovite transformation and calculation of the phase boundary. *Phys Chem Minerals, 23*, 11–16, doi:10.1007/BF00202988

Pugh, S., Jenkins, J., Boyce, A., & Cottaar, S. (2021). Global receiver function observations of the X-discontinuity reveal recycled basalt beneath hotspots. *Earth and Planetary Science Letters, 561*, 116813, doi:10.1016/j.epsl.2021.116813

Revenaugh, J., & Jordan, T. H. (1991). Mantle layering from ScS reverberations: 3. The upper mantle. *Journal of Geophysical Research: Solid Earth, 96* (B12), 19781–19810, doi:10.1029/91JB01487

Schmerr, N. (2015). Imaging mantle heterogeneity with upper mantle seismic discontinuities. *In A. Khan F. Deschamps (Eds.), The earth's heterogeneous mantle: A geophysical, geodynamical, and geochemical perspective* (pp. 79–104). Springer International Publishing, doi:10.1007/978-3-319-15627-9 3

Williams, Q., & Revenaugh, J. (2005). Ancient subduction, mantle eclogite, and the 300 km seismic discontinuity. *Geology, 33* (1), 1–4, doi:10.1130/G20968.1

Woodland, A. B. (1998). The orthorhombic to high-P monoclinic phase transition in Mg-Fe Pyroxenes: Can it produce a seismic discontinuity? *Geophysical Research Letters, 25* (8), 1241–1244, doi:10.1029/98GL00857

Xu, W., Lithgow-Bertelloni, C., Stixrude, L., & Ritsema, J. (2008). The effect of bulk composition and temperature on mantle seismic structure. *Earth and*

Planetary Science Letters, 275 (1), 70–79, doi:10.1016/j.epsl.2008.08.012

Yu, Y., Wu, Z., & Wentzcovitch, R. (2008). transformations in Mg_2SiO_4 in Earth's transition zone. *Earth Planet. Sci. Lett, 273*, 115–122, doi:10.1016/j.epsl.2008.06.023

Yu, Y. G., Wentzcovitch, R. M., Vinograd, V. L., & Angel, R. J. (2011). Thermodynamic properties of $MgSiO_3$ majorite and phase transitions near 660 km depth in $MgSiO_3$ and Mg_2SiO_4: A first principles study. *Journal of Geophysical Research (Solid Earth), 116* (B2), B02208, doi:10.1029/2010JB007912